Challenges in the Experimental Measurement and High-Fidelity Simulation of Turbulent Cavitation

Prof. Steve Ceccio
University of Michigan
Ann Arbor, MI, 48109
USA

ceccio@umich.edu

Prof. Krishnan Mahesh
University of Minnesota
Minneapolis, MN, 55455
USA

kmahesh@umn.edu

ABSTRACT

Turbulent cavitation, particularly in the inception and sheet to cloud transition regimes, presents formidable challenges to both controlled experimentation and high-fidelity simulations. Cavitating flows are of great practical interest since the highly unsteady flow can induce significant fluctuations in the thrust and torque of marine propellers, while the violent collapse of vapour clouds can cause material damage to the blades. We describe a study of sheet to cloud transition over a wedge by collaborative experiments performed at the University of Michigan and large-eddy simulation performed at the University of Minnesota. Observations of partial cavitation forming on the apex of a wedge was studied both experimentally and with numerical simulations. High-speed visualization and time resolved X-ray densitometry measurements were employed to examine the cavity dynamics, including the time resolve void fraction fields within the cavity, as described by Ganesh (2015) and Ganesh et al. (2016). Both UNRANS and LES were used to compute the cavity flow. The LES uses a novel numerical method developed by Gnanaskandan and Mahesh (2015); the homogeneous mixture model represents the multiphase mixture, a characteristic based filtering captures discontinuities and a dynamic Smagorinsky model represents small-scale turbulence. The paper will elaborate on details of the experiment, simulations, and their comparison. It will then outline the challenges posed in the validation and make recommendations for future experimental measurements that are essential in developing the reliable computational prediction of cavitating flows.

1.0 BACKGROUND

Cavitation can occur when the pressure in a liquid falls below the vapour pressure as a result of hydrodynamically or acoustically generated pressure fields. In many practical instances, vapour forms when small bubbles (*i.e.* nuclei) are present in a region of low or negative pressure (*i.e.* tension) and rapidly grow. If such vapour bubbles are then exposed to a recovering pressure, they can collapse violently. This leads to the production of strong noise emission, and the creation of shock waves and mechanical impulses at nearby flow boundaries. Cavitation has been associated with a variety of flow mechanisms that lead to steady or unsteady reductions in the fluid pressure. Turbulent flows are associated with regions of coherent vorticity and strong unsteady pressure fluctuations, and these flows can exhibit complex cavitating behaviour. Both wall bounded and free shear flows can cavitate. Under incipient conditions, the number and frequency of cavitating nuclei are few. But, as the cavitation number is reduced, the likelihood that regions of tension form in the turbulent flow increases, and the cores of the low-pressure vortices may begin to fill with vapour.

Prediction of incipient and developed cavitating turbulent flows remains a challenge. A key reason for the limited success to-date is that the onset of cavitation involves non-linear and often explosive interactions between free-stream and/or surface nuclei and unsteady pressure fields. Consequently, prediction of the conditions cavitation inception and development as well as the physical mechanisms associated with the creation of noise and pressure impulses requires quantitative understanding of the pressure field of the flow, which is spatially inhomogeneous for most flows of naval interest, and in the case of turbulent flows, unsteady and scale dependent. The so-called "water quality", which encompasses the nature, as well as the spatial and size distribution of free stream nuclei, along with the dissolved gas content, and surface tension is also an important factor, especially for incipient cavitation. These underlying physical processes can vary substantially for similar flows that span wide range of Reynolds numbers. Moreover, inception is often associated with the smallest (*e.g.* secondary) unsteady flow features that can be difficult to resolve in simulation across of wide range of Reynolds numbers.

Computation of cavitating flows is particularly challenging, especially for high Reynolds number turbulent flows. Steady–state RANS has traditionally been the simplest turbulence model and has been used to predict steady state quantities like cavity length and pressure. Unsteady RANS (URANS) has been successfully used in predicting some quantities in unsteady cavitation. For example, URANS predicts cloud-shedding frequency in sheet to cloud cavitation transition to a reasonable accuracy. However, even URANS does not predict all unsteady quantities and LES can potentially be used as a predictive tool in unsteady cavitation problems (Mahesh *et al.*, 2015).

In the present study, the authors experimentally examine and numerically compute a particular turbulent cavitating flow: partial cavitation. Partial cavitation occurs when the low-pressure regions produced by separated shear flows are filled with vapour, forming a cavity. Flow scenarios exhibiting partial cavitation are separated shear layers on the suction side of lifting surfaces at high attack angles, blades of turbo machinery, inducers of cryogenic rocket motors, and the passages of a diesel fuel injectors. Once formed, partial cavities can be stable, with a nominally constant length. But, partial cavities can also undergo auto oscillations of cavity length that are characterised by the shedding of vapour clouds, termed as cloud cavitation. The length of oscillation can be intermittent or periodic. Moreover, the presence of cloud cavitation can lead to unsteady loading, pressure pulsations, erosion, and severe degradation of system performance.

The authors and their collaborators developed a canonical geometry to study the formation and dynamics of a nominally two-dimensional partial cavity forming at the apex of a wedge. The experiments and computations were conducted simultaneously and jointly, and the preliminary results of each effort informed the other. Both

RANS and LES were used to perform the computations. Ultimately, the effort led to both a richer understanding of the flow physics and to insights into efficient and effective modelling strategies. This paper presents a summary of the effort as well as a discussion of lessons learned regarding the effective interaction of between experimentalists and those engaged in the development and validation of physics based numerical models. Portions of the results presented here have also been presented in Ganesh (2015), Ganesh *et al.* (2016), and Gnanaskandan and Mahesh (2016c)

2.0 FLOW GEOMETRY AND CONDITIONS

Experiments were carried out at the University of Michigan 9" Water Tunnel. The tunnel has a 6:1 round contraction leading into a test section with a diameter of 22 cm (9 inches), and the test section then transitions to a square cross section that is 21 cm by 21 cm with chamfered corners. The flow velocity and the static pressure in the tunnel test section can be varied from 0 to 18 m/s and from near vacuum to 100 kPa gauge pressure. A de-aeration system enables the control of the dissolved air content, but not the free gas content. For the present experiments, the test section was further reduced in area to a conduit that had a 7.6 cm by 7.6 cm cross-section. Figure 9-1 shows a schematic diagram of the wedge within the test section. The height of the wedge was 2.51 cm, with a length of 24 cm. The upstream and downstream surfaces are at angles of 21.8 and 8.1 degrees, respectively. A two-dimensional wedge was mounted in the reduced test section between the straight sidewalls of the tunnel, and optical access to the wedge was permitted through the use of acrylic test-section windows. The static pressure at the entrance of the secondary test section is measured using an Omega PX20-030A5V absolute pressure transducer, and the pressure difference between the test section inlet and upstream of the primary contraction was measured using an Omega PX409030DWU10V differential pressure transducer. The velocity at the entrance flow speed in to the reduced test section was calculated *via* the measurement of the differential pressure. A Laser Doppler Velocimeter (LDV) was used to measure the velocity profile 79 mm upstream of the wedge apex in transverse direction in the test section mid-plane. Figure 9-2 shows the data across the test section with D_{TS} = 76 mm, and shows the near wall boundary layer flow for U_{Max} = 1.85 m/s. These data and the inlet and outlet pressures of the test section were used as boundary conditions for the computational models.

The cavitating flow around the wedge was imaged with a Phantom v730 high-speed video camera. A 90 mm focal length lens was used to record a viewing area of 15.5 by 4.5 cm, and the flow was illuminated using Arrilux lamps. The frame rate of the video recordings was 4000 frames per second (fps), with a 35 microsecond exposure time, and the camera was triggered manually. Further details of the setup are provided by Ganesh (2015) and Ganesh *et al.* (2016).

The velocity at the inlet of the secondary test section was is U_O which is know to an uncertainty of ± 0.1 m/s, and the pressure upstream of the wedge at the inlet, p_O, was varied between 60 and 110 kPa. The freestream cavitation number, σ_o, is defined as

$$\sigma_O = \frac{p_O - p_V}{\frac{1}{2}\rho_l U_O^2} \tag{1}$$

where p_V is the vapour pressure of water, and ρ_l is water density. The uncertainty of σ_o is +/- 0.1. The dissolved oxygen content was maintained at approximately 50%, and the water temperature was T = 22 +/- 1 C.

A cinemagraphic X-ray densitometry system was used to measure the spatial distribution of void fraction for

the cavitating flow around the wedge. A complete description of the system is provided by Mäkiharju (2012) and Mäkiharju *et al.* (2013). The X-ray densitometry system had a source capable of 433 mA at 150 kV, and the imager system comprised of an image intensifier coupled with a high-speed camera (Vision Research Phantom V9.0). Note that the fraction of photons of any one specific photon energy that is not attenuated is related to the mass attenuation coefficients, densities and thicknesses of all the materials present along the path of the beam. Based on the Beer-Lambert law, for a domain with N distinct materials we can write

$$\frac{I}{I_0} = e^{\left(\sum_{i=1}^{N} (x_n \rho_n / \mu_n)\right)},$$

(2)

where I_0 is the original intensity of the photon beam, I is the intensity of the photons transmitted, μ_n / ρ_n is the mass attenuation coefficient, ρ_n is the density, x_n is the mass thickness of beam path through material n. The attenuation coefficient is a known property of photon energy and any material in the domain, and is related to the material density and its atomic properties (Hubbell and Seltzer, 2004). Therefore for a single material, $N = 1$, a measure of the change in intensity can be converted into a measure of the average density of the material along the beam path. And, in the case of two-phase gas-liquid flows, the path averaged void fraction, α, is given by

$$\alpha = \frac{\ln\left(\frac{I_m}{I_w}\right)}{\ln\left(\frac{I_a}{I_w}\right)}$$

(3)

as a function of the intensities, I, of photon fluxes having passed through a test section filled with a mixture "m", all water "w", or all air "a" at any one given photon energy. The accuracy of the void fraction measurement has been validated against those obtained by use of water phantoms representative of the observed void fractions. Water phantoms were used to calibrate for void fraction, and this calibration sets the maximum gray-scale value for the camera. The RMS uncertainty of absolute void fraction for any pixel in a single (non-time averaged) frame is approximately $\alpha = +/- 0.05$, and the uncertainty of the mean void fraction is $\alpha = +/-0.01$.

3.0 EXPERIMENTAL RESULTS

Cavitation patterns occurring on the wedge was studied by systematically varying the cavitation number and free-stream speed. The wide-ranging results of this study are reported in Ganesh (2015) and Ganesh *et al.* (2016). The cavity flow undergoes a variety of dynamics as the cavitation number is reduced. Specifically, the shorter more stable cavities forming at the wedge apex grow with decreasing σ_o. When the cavitation number reached a value close to $\sigma_o = 2.1$, the experimental cavities exhibited tendencies to shed, by shedding intermittent clouds of vapour. Such cavities are termed as "transitory cavities". With a further reduction in cavitation number, more rigorous and periodic shedding was observed. The transition from transitory to "periodic cavities" is related to the change in shedding mechanism from re-entrant flow to the propagation of bubbly shocks.

For comparison to the computations, we consider a transitory cavity occurring at a cavitation number of $\sigma_o = 2.1$. The transitory cavity had average length of about 30% of the length of the wetted surface of the wedge

downstream from the apex. Images from a time series of cavity recorded using a high speed video camera at 5000 frames per second from the top and side view are shown in Figure 9-3. Under these conditions, the cavity has a nominally steady average length, with variation due to the shedding of smaller cavities in the region of the cavity closure. This is in contrast to the shock-induced shedding that occurs at lower σ_∞ when the cavity undergoes complete pinch-off at the wedge apex (*e.g.* it has undergone sheet to cloud transition). Here the scales are normalized with the streamwise length of the wedge surface downstream of the apex, $L_W = 178$ mm.

Figure 9-4 presents instantaneous images of the void fraction field, and two different shedding mechanisms are illustrated. In the first, the small-scale cavity shedding is associated with re-entrant flow in the cavity closure region. In the second, the formation of a bubbly shock wave within the cavity propagates upstream and impinges on the cavity leading edge, resulting in large-scale shedding of a vapour cloud. As discussed in Ganesh *et al*. (2016), transitory cavities are less likely to experience the shock-induced shedding process, since the local *average* Mach number with the flow is subsonic. Figure 9-5 presents time averaged and RMS void fraction field images of the void fraction field, and two different shedding mechanisms are illustrated. These data will be used for comparison to the RANS and LES models discussed below.

4.0 COMPUTATION OF THE FLOW

Two methods are used to compute the transitional cavity flow around the wedge. Both use the homogeneous mixture model that assumes the mixture of constituent phases to be a single compressible fluid. Surface tension effects are assumed small and are neglected. The governing equations are the compressible Navier Stokes equation for the mixture of liquid and vapor along with a transport equation for vapor. The density of the homogeneous mixture, ρ, is given by

$$\rho = \rho_l(1 - \alpha) + \rho_g \alpha, \tag{4}$$

where ρ_l and ρ_g are the density of the liquid and gas, respectively, and α is the void fraction. The mass vapor fraction, Y, is given by

$$\rho_l(1 - \alpha) = \rho(1 - Y) \quad \text{and} \quad \rho_g \alpha = \rho Y. \tag{5}$$

The transport equation for the mass vapor fraction is given by

$$\frac{\partial \rho Y}{\partial t} = -\frac{\partial}{\partial x_k}(\rho Y u_k) + S_e - S_c, \tag{6}$$

where S_e and S_c are the evaporation of liquid and condensation of the vapor. These are given by

$$S_e = C_e \alpha^2 (1 - \alpha)^2 \frac{\rho_l}{\rho_g} \frac{\max(p_v - p, 0)}{\sqrt{2\pi R_g T}},$$

$$S_c = C_c \alpha^2 (1 - \alpha)^2 \frac{\max(p - p_v, 0)}{\sqrt{2\pi R_g T}}, \tag{7}$$

where p_V is the vapor pressure, $R_g = 461:6$ J /kg K, and T is the mixture temperature. C_e and C_c are empirical constants with values assumed to be 0.1 (Saito *et al.*, 2007). Finally, the equation of state for the pressure, p,

$$p = Y\rho R_g T + (1-Y)\rho K_l T \frac{p}{p+P_c}.$$

(8)

where $K_l = 2684.075$ J / kg K and $P_c = 786:333$ x 10^6 Pa. Details are provided by Gnanaskandan and Mahesh (2015). This homogeneous mixture model of the multiphase flow is used in both the Large Eddy Simulation (LES) and the Unsteady Reynolds Averaged Navier Stokes (UNRANS) computations to follow.

4.1 LES Formulation

The LES formulation starts with Favre spatial filtering of the governing equations

$$\frac{\partial \overline{\rho}}{\partial t} = -\frac{\partial}{\partial x_k}\left(\overline{\rho}\tilde{u}_k\right),$$

$$\frac{\partial \overline{\rho}\tilde{u}_i}{\partial t} = -\frac{\partial}{\partial x_k}\left(\overline{\rho}\tilde{u}_i\tilde{u}_k + \overline{p}\delta_{ik} - \tilde{\sigma}_{ik} - \tau_{ik}\right),$$

$$\frac{\partial \overline{\rho}\tilde{Y}}{\partial t} = -\frac{\partial}{\partial x_k}\left(\overline{\rho}\tilde{Y}\tilde{u}_k - t_k\right) + \tilde{S}_e - \tilde{S}_c,$$

$$\frac{\partial \overline{\rho}\tilde{e}_s}{\partial t} = -\frac{\partial}{\partial x_k}\left(\overline{\rho}\tilde{e}_s\tilde{u}_k - \tilde{Q}_k - q_k\right) - \overline{p}\frac{\partial \tilde{u}_k}{\partial x_k} + \tilde{\sigma}_{ik}\frac{\partial \tilde{u}_i}{\partial x_k}$$

(9)

were the tilde quantities are Favre averaged quantities and τ_{ik}, q_k and t_k are subgrid scale (SGS) stress, heat flux and scalar flux. These terms are modeled using the Dynamic Smagorinsky model (DSM)

$$\tau_{ij} - \frac{\delta_{ij}}{3}\tau_{kk} = -2C_S(\mathbf{x},t)\overline{\rho}\Delta^2\left|\tilde{S}\right|\widetilde{S^*_{ij}},$$

$$\tau_{kk} = 2C_I(\mathbf{x},t)\overline{\rho}\Delta^2\left|\tilde{S}\right|^2,$$

$$q_i = -\overline{\rho}\frac{C_S(\mathbf{x},t)\Delta^2\left|\tilde{S}\right|}{Pr_T}\frac{\partial \overline{T}}{\partial x_i},$$

$$t_i = -\overline{\rho}\frac{C_S(\mathbf{x},t)\Delta^2\left|\tilde{S}\right|}{Sc_T}\frac{\partial \overline{Y}}{\partial x_i},$$

(10)

where $|S| = \sqrt{2S_{ij}S_{ij}}$ and $S^*_{ij} = S_{ij} - 1/3S_{kk}\delta_{ij}$. The model coefficients C_S, C_I, Pr_T, and Sc_T are determined using the Germano identity,

$$
\begin{aligned}
C_S \Delta^2 &= \frac{1}{2} \frac{\langle L_{ij}^* M_{ij}^* \rangle}{\langle M_{ij}^* M_{ij}^* \rangle}, \\
L_{ij}^* &= \left(\frac{\widehat{\overline{\rho u_i} \cdot \overline{\rho u_j}}}{\overline{\rho}} \right) - \frac{\widehat{\overline{\rho u_i}} \cdot \widehat{\overline{\rho u_j}}}{\widehat{\overline{\rho}}}, \\
M_{ij}^* &= \overline{\rho} \widehat{|\tilde{S}| \tilde{S}_{ij}^*} - \widehat{\overline{\rho}} \left(\frac{\widehat{\Delta}}{\Delta} \right)^2 |\widehat{\tilde{S}}| \widehat{\tilde{S}_{ij}^*},
\end{aligned}
$$
(11)

where $\langle \cdot \rangle$ denotes spatial average over neighboring control volumes and the caret denotes test filtering. Test filtering is defined by the linear interpolation from face values of a control volume, which is again the interpolation from two adjacent cell center values (Park and Mahesh, 2007):

$$
\widehat{\phi} = \frac{1}{N_{\text{face}}} \sum_{\text{no of face}} \phi_f = \frac{1}{2 N_{\text{face}}} \sum_{\text{no of face}} (\phi_{icv1} + \phi_{icv2}),
$$
(12)

where N_{face} is the number of faces for a given control volume. Further details are provided in Gnanaskandan and Mahesh (2016a)

5.2   URANS Formulation

The URANS formulation employs the Spalart-Allmaras model (Spalart and Allmaras,1992).

$$
\frac{\partial \rho \tilde{\nu}}{\partial t} + \frac{\partial (\rho \tilde{\nu} u_k)}{\partial x_k} = c_{b1} \tilde{S} \rho \tilde{\nu} +
$$
$$
\frac{1}{\sigma} [(1 + c_{b2}) \nabla \cdot ((\rho \nu + \rho \tilde{\nu}) \nabla \tilde{\nu}) - c_{b2} (\rho \nu + \rho \tilde{\nu}) \nabla \cdot \nabla \tilde{\nu}]
$$
$$
- \rho c_{w1} f_w \left(\frac{\tilde{\nu}}{d} \right)^2 .
$$
(13)

where $\nu_T = \tilde{\nu} f_{v1}$, $f_{v1} = \chi^3 / (\chi^3 + c_{v1})$ an $\chi = \tilde{\nu}/\nu$ v . S is the strain rate tensor. The model is closed with the following coefficients and wall functions:

$$
\begin{aligned}
&\tilde{S} = S + \frac{\tilde{\nu}}{\kappa^2 d^2} f_{v2}, \quad f_{v2} = \left(1 + \frac{\chi}{c_{v2}} \right)^{-3}, \\
&f_w = g \left(\frac{1 + c_{w3}^6}{g^6 + c_{w3}^6} \right)^{1/6}, \quad g = r + c_{w2}(r^6 - r), \quad r = \frac{\tilde{\nu}}{\tilde{S} \kappa^2 d^2}, \\
&c_{b1} = 0.1355, \quad \sigma = \tfrac{2}{3}, \quad c_{b2} = 0.622, \quad \kappa = 0.41, \quad c_{v2} = 5, \\
&c_{w1} = \frac{c_{b1}}{\kappa^2} + \frac{1 + c_{b2}}{\sigma}, \quad c_{w2} = 0.3, \quad c_{w3} = 2, \quad c_{v1} = 7.1.
\end{aligned}
$$
(14)

For cavitating flows, Coutier-Delgosha *et al.* (2003) observed that the eddy viscosity obtained from standard RANS models can be excessive, especially near the cavity closure region, which prevents cloud formation.

Hence they suggested that the eddy viscosity be modified near the cavity interface as

$$\mu_T = \nu_T \left[\rho_g + (\rho_l - \rho_g)(1-\alpha)^{10} \right].$$

(15)

Once ν_T is computed, the Reynolds stresses are given by

$$\mathcal{R}_{ij} = -2\rho\nu_T\overline{S}_{ij}.$$

(16)

The turbulent thermal conductivity and turbulent scalar diffusivity are also computed from the eddy viscosity assuming a turbulent Prandtl number $Pr_t = 0.9$ and a turbulent Schmidt number $Sc_t = 0.7$. The turbulent scalar equation is then modified as

$$\frac{\partial \rho Y}{\partial t} = -\frac{\partial}{\partial x_k}(\rho Y u_k) + S_e - S_c + \frac{\partial}{\partial x_k}\left(\frac{\nu_t}{Sc_t}\frac{\partial \rho Y}{\partial x_k}\right).$$

(17)

Solution of these equations is detailed by Gnanaskandan and Mahesh (2015). The algorithm has been validated for a variety of flows including a cavitating shock tube, turbulent cavitating flow over a hydrofoil (Gnanaskandan and Mahesh, 2014 and 2015) and a hemispherical headform (Gnanaskandan and Mahesh, 2016b).

5.0 COMPUTATIONAL RESULTS

These methods were used to compute the transitional partial cavity flow described in Section 3. In order to minimize the effect of acoustic reflection from the boundaries, the computational domain is extended in both upstream ($25h$) and downstream directions ($50h$), where $h = 2.5$ cm is the height of the wedge. Moreover, acoustically absorbing boundary conditions were applied in the manner described by Colonius (2004). The velocity and pressures are prescribed at the inlet and downstream pressure is prescribed at the outlet. No slip boundary conditions are imposed on top and bottom walls. Periodic boundary conditions are enforced at the spanwise boundaries. The Reynolds number of the flow based on the wedge height h, and a bulk velocity of U_O = 8 m/s is approximately $Re = 0.2 \times 10^6$ and the cavitation number is $\sigma_O = 2.1$. The mesh is made very fine near the wedge apex and along the entire length of the wedge where the major portion of the vapor is expected to form. The minimum grid spacing near the wedge is $0.001h \times 0.001h$ in the wall normal and streamwise directions respectively. The wall normal spacing stretches to $0.005h$ at a height of $0.5h$ from the wedge apex and further to about $0.01h$ at a height of h from the apex. In the streamwise direction, the grid is stretched to $0.02h$ at a distance $3.5h$ from the apex and further to $0.01h$ at the end of the wedge. The LES grid has 80 points in the spanwise direction.

The time-averaged values in the simulations are obtained by performing time average over four shedding cycles. For the LES simulations, further convergence is obtained by averaging along the statistically homogeneous spanwise direction as well. Figure 9-6 shows the mean void fraction contours obtained from experiment, LES and URANS. A good agreement is obtained for cavity length and the value of mean void fraction inside the cavity between LES and experiment. The URANS simulation predicts a larger cavity length. The cavity thickness predicted by LES is slightly larger than the experimental measurement while that predicted by URANS is even larger than LES. Thus LES does a better job in predicting the cavity dimensions.

The mean void fraction at different streamwise locations on the wedge obtained from LES and URANS are compared to the experimental results in Figure 9-7. Note the overall good agreement of the value of mean void fraction inside the cavity for LES in contrast to unsteady RANS. Further, the length of the cavity is also not predicted well by unsteady RANS, while LES gives an excellent agreement for the mean length. The thickness is slightly mispredicted by LES at stations $x/h = 1.0$ and $x/h = 2.0$, while the thickness predicted by unsteady RANS is even worse. Overall, LES agrees much better with the experiments than unsteady RANS. The uncertainty of the experimentally measured mean void fraction is +/- 0.01.

Next we compare the RMS of void fraction obtained from simulations and experiment in Figure 9-8. Only the resolved portion of the fluctuation obtained from LES is shown here, and the uncertainty in the instantaneous void fraction is +/- 0.05. Hence, the free stream fluctuation measured in the experiment does not go to zero while that predicted by LES and URANS goes to zero away from the cavity. The qualitative trend from LES agrees well with the experiment at all the stations and LES also seems to predict the RMS much better than unsteady RANS. The fact that LES predicts a thicker cavity is also manifested in the form of higher magnitude of fluctuations away from the wedge. Overall, the comparisons for void fraction data are encouraging suggesting the suitability of LES in predicting this highly unsteady phenomenon.

Two quantities are defined are defined

$$\overline{\sigma}_{loc} = 2(\overline{p} - p_v)/\rho_\infty u_\infty^2 \tag{18}$$

and

$$\sigma' = 2\sqrt{\overline{p'^2}}/\rho_\infty u_\infty^2 \tag{19}$$

to compare the local cavitation characteristics. Figure 9-9(a) and (b) show the variation of these values along the wedge, where $x / h = 0$ is the apex region and minimum $\overline{\sigma}_{loc}$ is obtained there. It is interesting to see that the mean pressure never falls below the vapor pressure for both LES and RANS, but the fluctuations at the apex are large enough for the instantaneous local pressure to fall below vapor pressure. Note that the value of RMS of pressure is maximum $x / h = 2.5$ which corresponds to the mean closure location of the cavity. This behavior points to cavity oscillation about that position. Interestingly, URANS predicts larger local cavitation number at the inception location, which points to higher mean pressure in that region. However, the pressure fluctuation at the apex predicted by URANS is about three times that predicted by LES. Further URANS consistently predicts higher fluctuation values leading to an increased amount of vapor production. Interestingly the RMS of vapor fraction predicted by URANS is higher than that of LES. Thus there is a consistent trend of all fluctuation quantities being over predicted by URANS.

Figure 9-10(a) and (b) shows the variation of mean density and mean volume fraction along the wedge. It is clear that inception occurs at the apex and the maximum amount of vapor in the mean flow occurs inside the sheet cavity. The region corresponding to the cloud has lesser void fraction than that in the sheet. This observation is also in line with the observations of Coutier-Delgosha et al. (2007). URANS predicts lesser mean vapor fraction immediately after inception near the wall. However as we move downstream URANS predicts more vapour closer to the wall than LES. Overall, LES agrees better with experiments when compared to URANS.

6.0 CONCLUSIONS

In the present paper we review some results from a simultaneous experimental and numerical examination of partial cavity flows over a wedge performed at the University of Michigan and large-eddy simulation performed at the University of Minnesota. Observations of partial cavitation forming on the apex of a wedge was studied both experimentally and with numerical simulations. High-speed visualization and time resolved X-ray densitometry measurements were employed to examine the cavity dynamics, including the time resolve void fraction fields within the cavity, as described by Ganesh (2015) and Ganesh et al. (2016).

Both URANS and LES were used to compute the cavity flow. The LES uses a novel numerical method developed by Gnanaskandan and Mahesh (2015); the homogeneous mixture model represents the multiphase mixture, a characteristic based filtering captures discontinuities and a dynamic Smagorinsky model represents small-scale turbulence. The comparisons between URANS and LES show a stark contrast in the unsteady sheet to cloud cavitation over a wedge. LES predicts both mean and RMS of void fraction inside the vapor cavity and near the cavity closure to a much better accuracy than URANS. It is also observed that URANS predicts much higher fluctuations for almost all quantities that might explain the discrepancy with the experimental results.

Simulations of cavitating flow can have several sources of empiricism; it is often difficult to separate the error due to the physical model from numerical error or the RANS/LES description. Also, it is not entirely satisfying to only evaluate cavitating simulations using surface pressure, loads or isocontours of volume fraction to identify cavity shape. The above comparative study was motivated by the need to go beyond these limitations, and is a first step in this direction. The study revealed the extreme sensitivity of internal cavitating flows to boundary conditions, especially for pressure; entirely different solutions can be obtained if pressure fluctuations are not properly propagated out of the domain boundaries. At the very least, pressure tap measurements of unsteady wall pressure both upstream and downstream, as done in the present study are crucial. Free-stream volume fraction is another input to simulations; at the very least data on its mean value is important. The solutions appear not to depend upon the details of the upstream boundary layer in the sheet to cloud regime but this observation need not be the same over all regimes, and requires closer examination. Accurate description of the upstream velocity field would therefore also be important for future studies. And finally, extension of the volume fraction measurements to three-dimensions and towards the near-wall region would great assist future comparative studies.

ACKNOWLEDGEMENTS

REFERENCES

[1] Colonius, T. "Modeling artificial boundary conditions for compressible flow". *Annual Review of Fluid Mechanics*, 36:315–345, 2004.

[2] Coutier-Delgosha, O., Stutz, B., Vabre, A., and Legoupil, S. "Analysis of cavitating flow structure by experimental and numerical investigations". *Journal of Fluid Mechanics*, 578:171–222, 2007.

[3] Ganesh, H. *Bubbly shock propagation as a cause of sheet to cloud transition of partial cavitation and stationary cavitation bubbles forming on a delta wing vortex.* Ph. D. thesis, University of Michigan, 2015.

[4] Ganesh, H., Mäkiharju, S. A., and Ceccio, S. L. "Bubbly shock propagation as a mechanism for sheet-to-cloud transition of partial cavities" *Journal of Fluid Mechanics*, 802:37-78, 2016.

[5] Gnanaskandan, A. and Mahesh, K. "A numerical method to simulate turbulent cavitating flows". *International Journal of Multiphase Flow*, 70:22–34, 2015.

[6] Gnanaskandan, A. and Mahesh, K. "Large eddy simulation of sheet to cloud cavitation". In *Proceedings of the 30th Symposium on Naval Hydrodynamics*, pages 1–13, 2014.

[7] Gnanaskandan, A. and Mahesh, K. "Large eddy simulation of the transition from sheet to cloud cavitation over a wedge". *International Journal of Multiphase Flow*, 83:86–102, 2016a.

[8] Gnanaskandan, A. and Mahesh, K. "Numerical investigation of near–wake characteristics of cavitating flow over a circular cylinder". *Journal of Fluid Mechanics*, 790, 2016b.

[9] Gnanaskandan, A. and Mahesh, K. "Comparative study of RANS and LES in simulating cavitating flows". *Proceedings of the 31st Symposium on Naval Hydrodynamics* (to appear).

[10] Hubbell, J.H. and Seltzer, S.M., 2004. "Cross section data for electron–positron pair production by photons: a status report." *Nuclear Instruments and Methods in Physics Research Section B: Beam Interactions with Materials and Atoms*, 213: 1-9.

[11] Mäkiharju, S.A., Gabillet, C., Paik, B.G., Chang, N.A., Perlin, M. and Ceccio, S.L., 2013. "Time-resolved two-dimensional X-ray densitometry of a two-phase flow downstream of a ventilated cavity." *Experiments in Fluids*, 54(7): 1-21.

[12] Mäkiharju, S.A., *The dynamics of ventilated partial cavities over a wide range of Reynolds numbers and quantitative 2D X-ray densitometry for multiphase flow.* Ph. D. thesis, University of Michigan, 2012.

[13] Park, N. and Mahesh, K. "Numerical and modeling issues in LES of compressible turbulence on unstructured grids". In *Proceedings of the 45th AIAA Aerospace Sciences Meeting and Exhibit*, AIAA Paper, number 0722: 1–18, 2007.

[14] Saito, Y., Takami, R., Nakamori, I., and Ikohagi, T. "Numerical analysis of unsteady behavior of cloud cavitation around a NACA0015 foil". *Computational Mechanics*, 40(1):85–96, 2007.

[15] Spalart, P. R. and Allmaras, S. R. "A one equation turbulence model for aerodynamic flows". *AIAA Journal*, 94(439): 1–22, 1992.

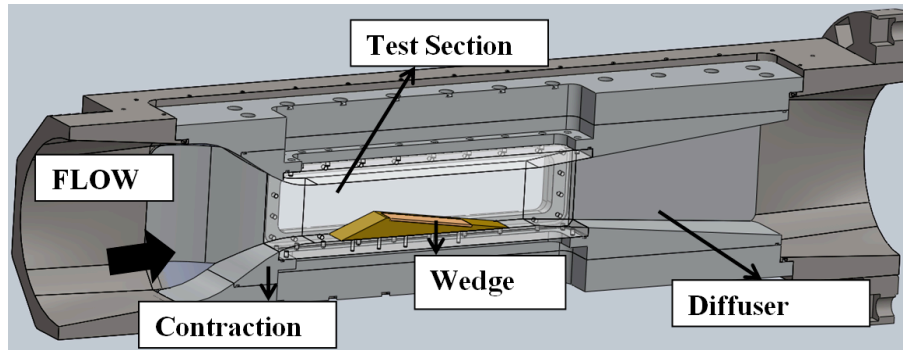**Figure 9-1: A drawing of the wedge and secondary test section installed the 9-Inch Water Channel.**

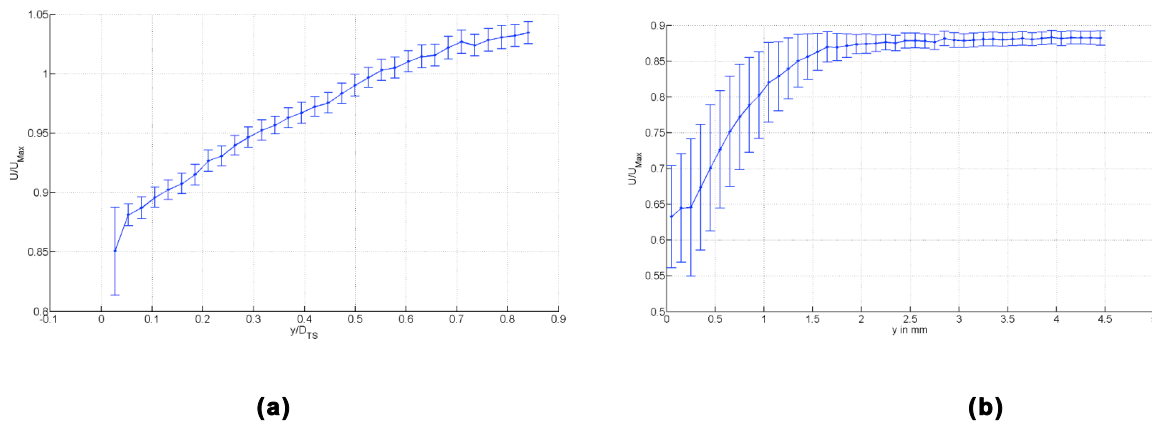**(a)**   **(b)**

Figure 9-2: LDV measurements of velocity profile 79 mm upstream of the wedge apex in the transverse direction on the test section mid-plane; (a) shows the data across the test section with D_{TS} = 76 mm, and (b) shows the near wall boundary layer. U_{Max} = 1.85 m/s.
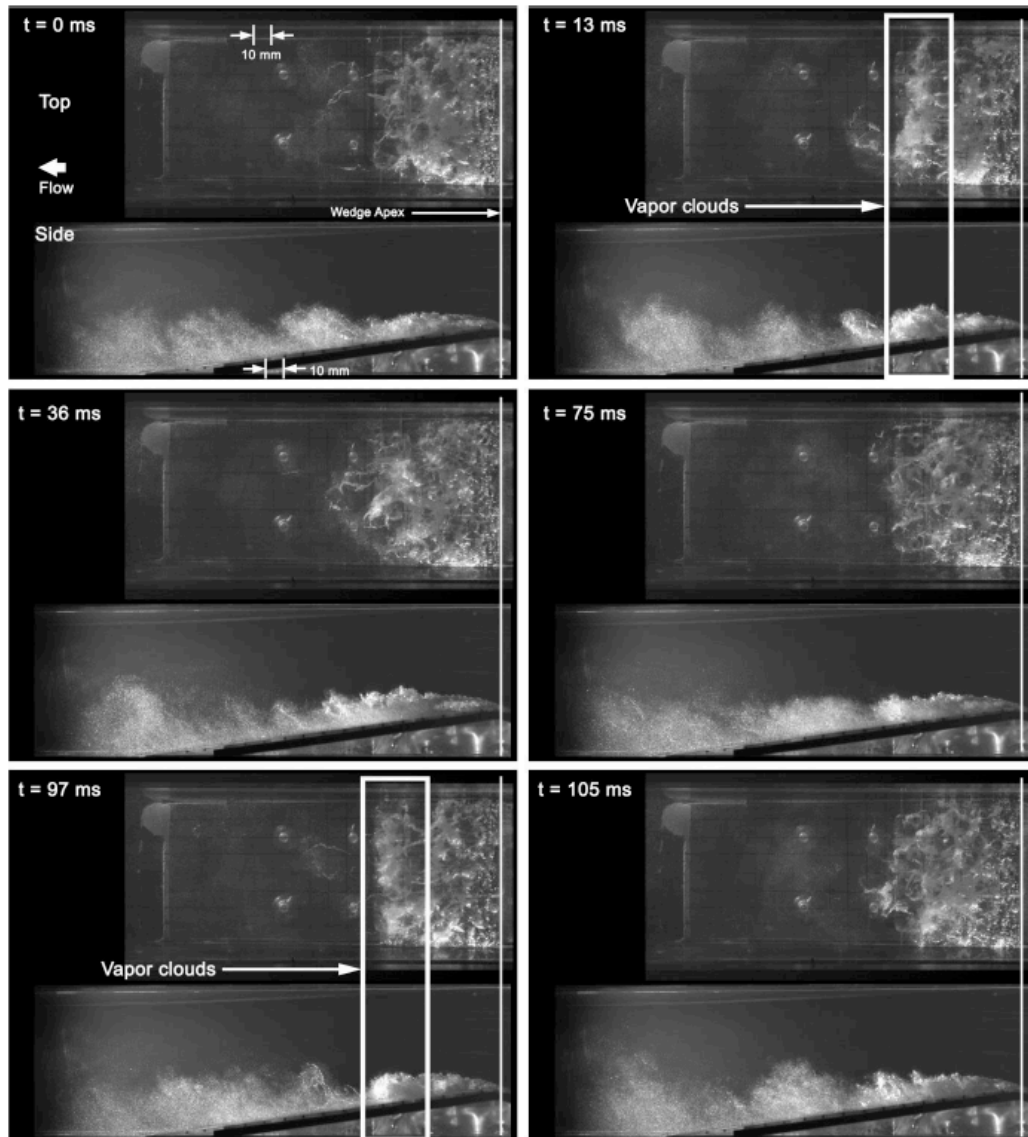
Figure 9-3: Images of the transitory cavity for σ_o = 2.1 and U_O = 8 m/s. Top and side views are time synchronised.
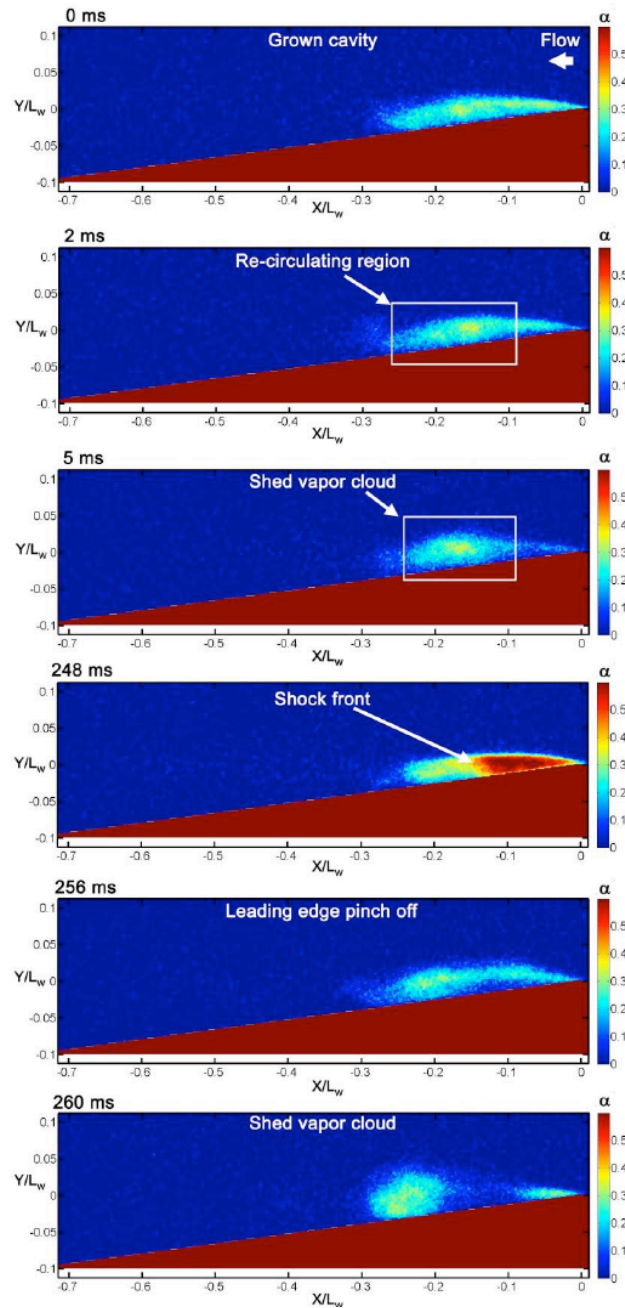
**Figure 9-4: Time evolution of the span-wise averaged void fraction field of the
transitory cavity for σ_o = 2.1 and U_O = 8 m/s. L_W = 178 mm is the streamwise length of
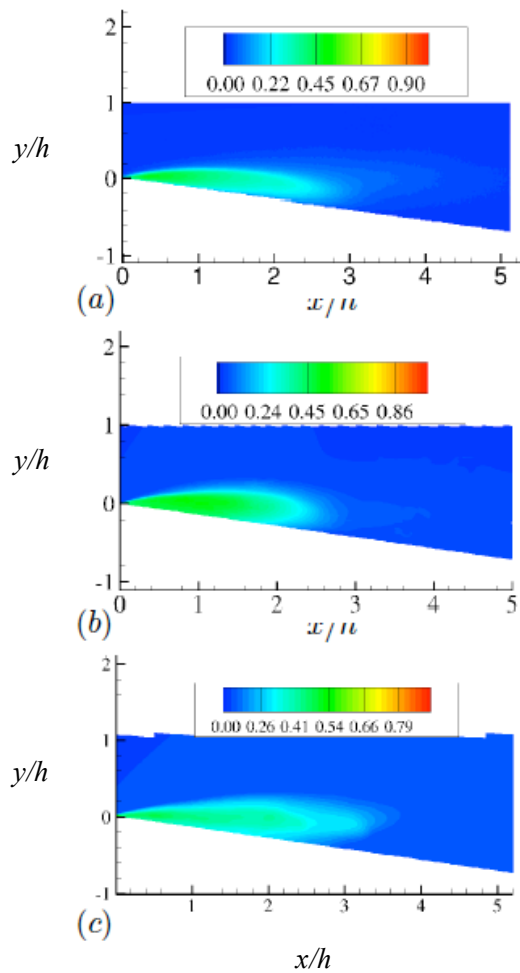the wedge surface downstream of the apex.**

(a)

(b)
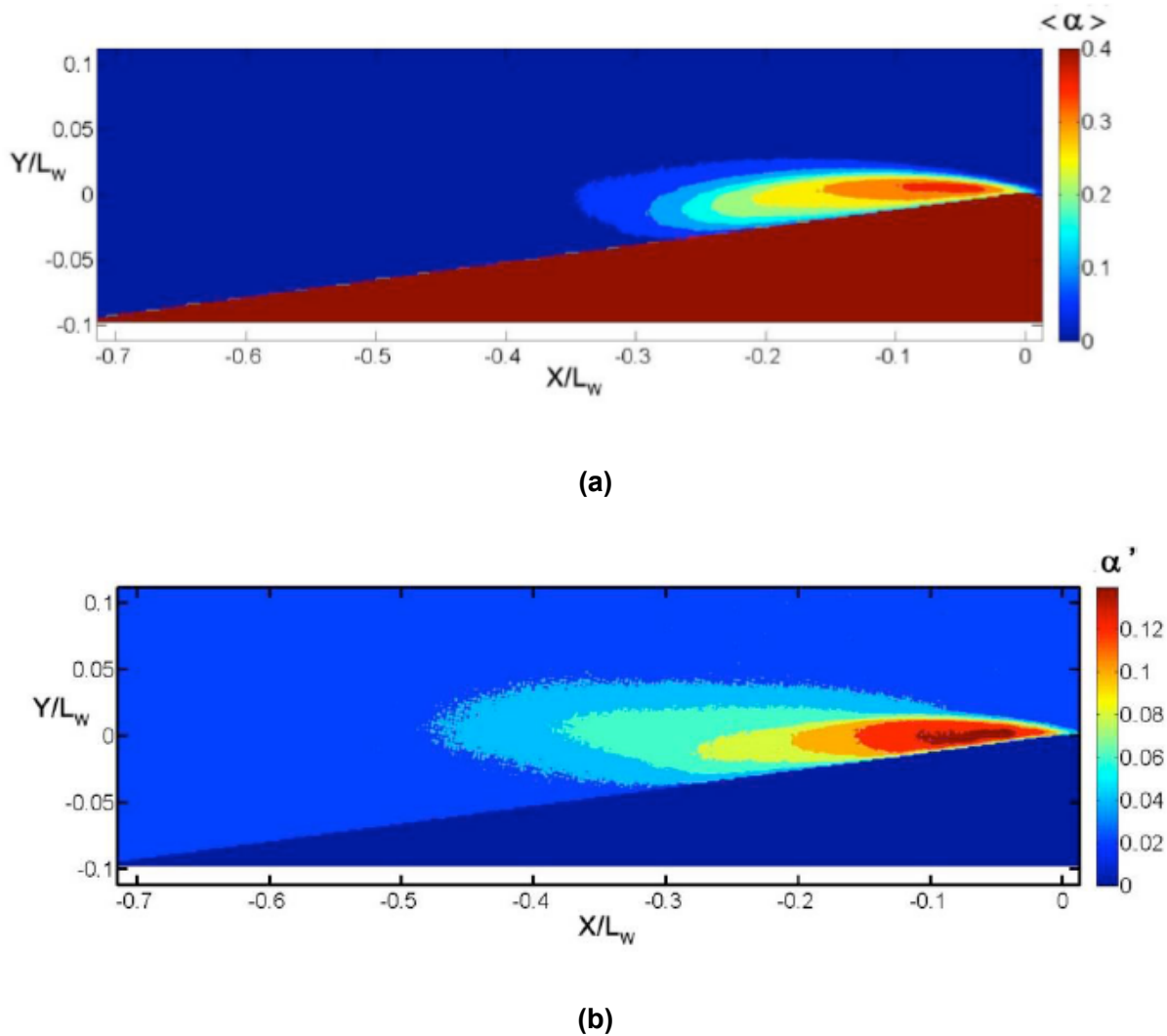
Figure 9-5: The (a) time averaged and (b) RMS of the span-wise averaged void fraction field, α, of the transitory cavity for σ_o = 2.1 and U_o = 8 m/s. L_w = 178 mm is the streamwise length of the wedge surface downstream of the apex.

Figure 9-6: Comparison of mean void fraction contours with (a) Experiment, (b) LES and (c) URANS for the transitory cavity for σ_o = 2.1 and U_O = 8 m/s. h = 2.6 mm is the step height.
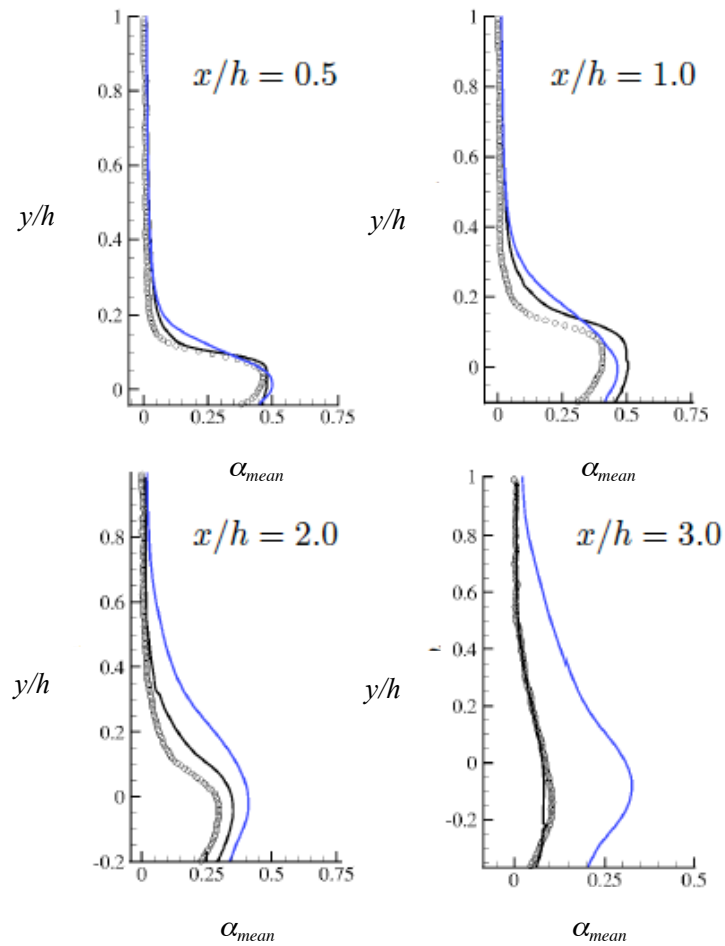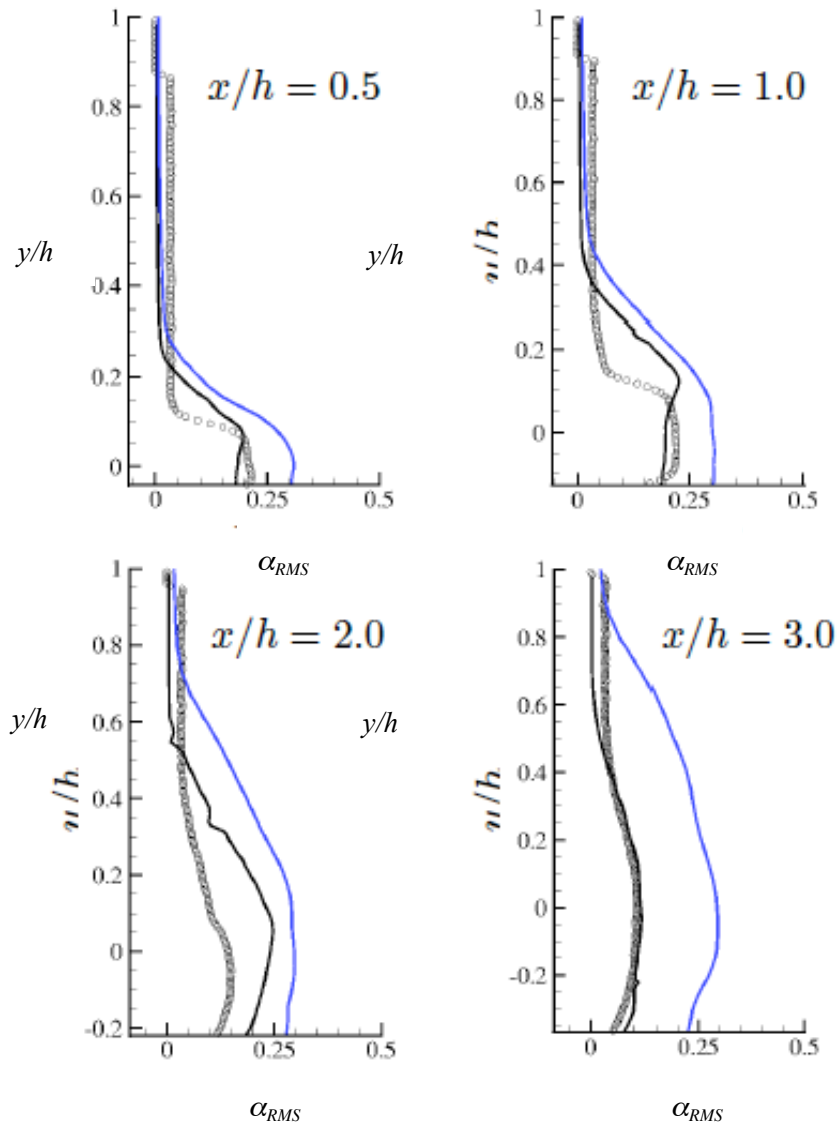
Figure 9-7: Comparison of mean void fraction profiles with (a) Experiment (o), (b) LES (black line) and (c) URANS (blue line) for the transitory cavity for σ_o = 2.1 and U_O = 8 m/s. h = 2.6 mm is the step height. The uncertainty of the experimentally measured mean void fraction is +/- 0.01.
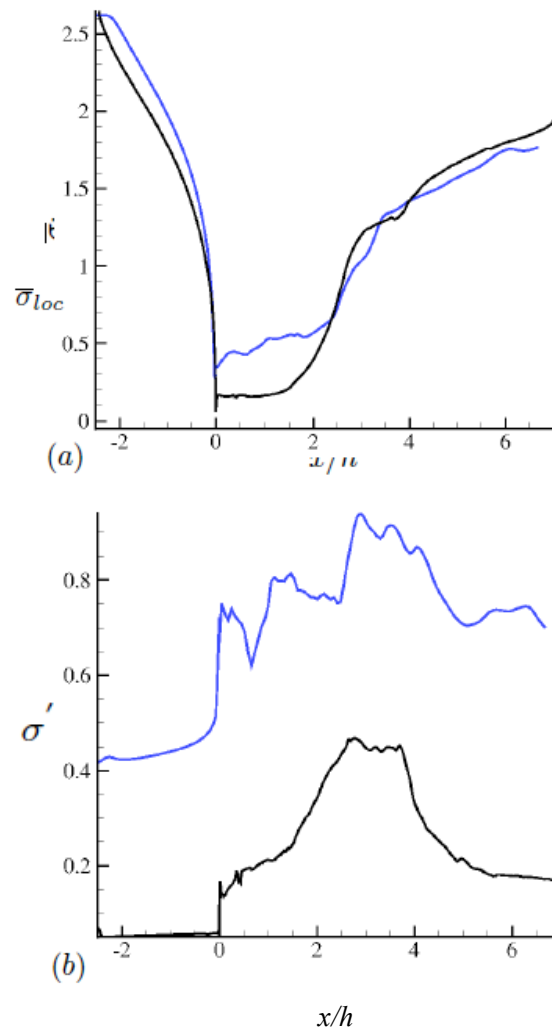
Figure 9-8: Comparison of RMS void fraction profiles with (a) Experiment (o), (b) LES (black line) and (c) URANS (blue line) for the transitory cavity for σ_o = 2.1 and U_O = 8 m/s. h = 2.6 mm is the step height. The uncertainty of the experimentally measured mean void fraction is +/- 0.05.

Figure 9-9: Variation of the local mean (a) and fluctuating (b) cavitation number along the wedge wall with the LES (black line) and URANS solutions for the transitory cavity for σ_o = 2.1 and U_o = 8 m/s. h = 2.6 mm is the step height.
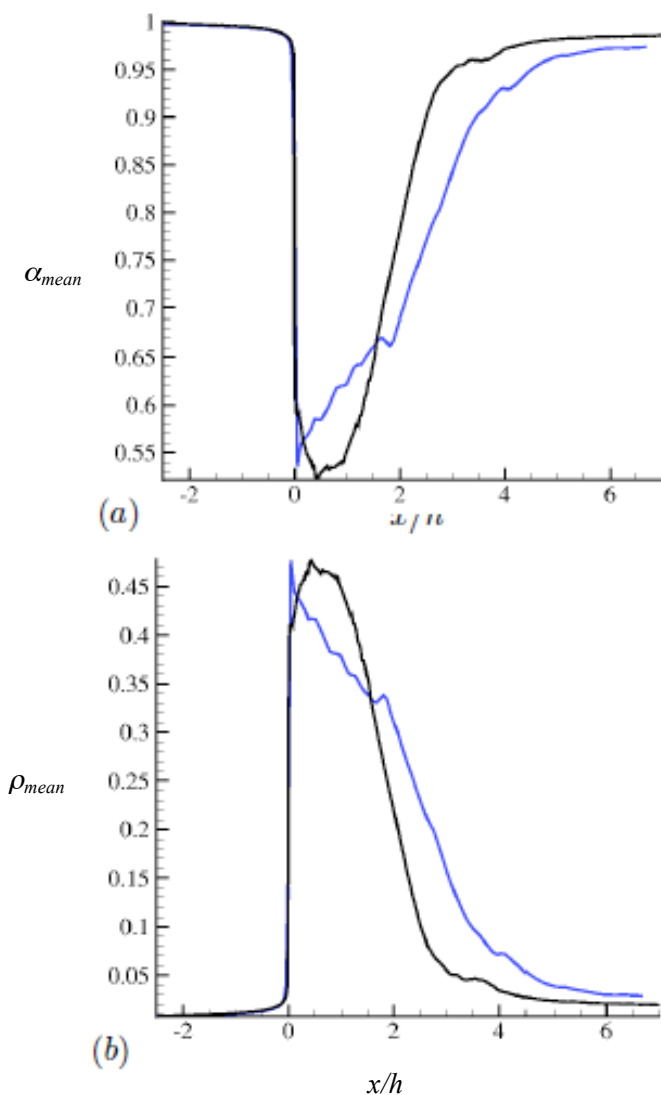
Figure 9-1-: Variation of the mean density (a) and mean void fraction (b) along the wedge wall with the LES (black line) and URANS solutions for the transitory cavity for σ_o = 2.1 and U_0 = 8 m/s. h = 2.6 mm is the step height.